Ionic Nickel Embedded in Ceria with High Specific CO2 Methanation Activity

Ionic Nickel Embedded in Ceria with High Specific CO_2 Methanation Activity

Mathias Barreau[1], Davide Salusso[2], Juan Li[3], Jinming Zhang[1], Elisa Borfecchia[4], Kamil Sobczak[5], Luca Braglia[6], Jean-Jacques Gallet[7,8], Piero Torelli[6], Hua Guo[9], Sen Lin[3] and Spyridon Zafeiratos[1,10,*]

[1]*Institut de Chimie et Procédés pour l'Energie, l'Environnement et la Santé, ICPEES UMR 7515 CNRS-Université de Strasbourg, 25 Rue Becquerel, 67087 Strasbourg, France*

[2]*European Synchrotron Radiation Facility, CS 40220, 38043 Grenoble Cedex 9, France*

[3]*State Key Laboratory of Photocatalysis on Energy and Environment, College of Chemistry, Fuzhou University, Fuzhou 350002, China*

[4]*Department of Chemistry, INSTM Reference Center and NIS Centers, University of Torino, 10125 Torino, Italy*

[5]*Faculty of Chemistry, Biological and Chemical Research Centre, University of Warsaw, Zwirki, Wigury 101, 02-089 Warsaw, Poland*

[6] *IOM CNR Laboratorio TASC, AREA Science Park, Basovizza, Trieste, 34149, Italy*

[7]*Laboratoire de Chimie Physique-Matière et Rayonnement, Sorbonne Université, Campus Curie, CNRS UMR 7614, 4 place Jussieu, 75005 Paris, France*

[8]*Synchrotron SOLEIL, L'orme des Merisiers, B.P. 48, Saint Aubin, Gif-sur-Yvette Cedex 91192, France*

[9]*Department of Chemistry and Chemical Biology, University of New Mexico, Albuquerque, New Mexico, 87131, USA*

[10]*School of Environmental and Chemical Engineering, Shanghai University, Shanghai, China*

CO_2 hydrogenation to methane is gaining increasing interest as one of the most promising ways to store intermittent renewable energy in the form of chemical fuels. Ni particles supported on CeO_2 represents a highly efficient, stable and inexpensive catalyst for this reaction. Herein, Ni-doped CeO_2 nanoparticles were tested for CO_2 methanation showing an extremely high Ni mass-specific activity and CH_4 selectivity. Operando characterization reveals that this performance is tightly associated with ionic Ni and Ce^{3+} surface sites, while formation of metallic Ni does not seem to considerably promote the reaction. Theoretical calculations confirmed the stability of interstitial ionic Ni sites on ceria surfaces and highlighted the role of Ce-O frustrated Lewis pair (FLP), Ni-O classical Lewis pair (CLP) and Ni-Ce pair sites to the activation of H_2 and CO_2 molecules. To a large extent, the theoretical predictions were validated by in situ spectroscopy under H_2 and CO_2:H_2 gaseous environments.

* spiros.zafeiratos@unistra.fr

Introduction

In 2021 the global CO_2 emissions from fossil fuel combustion and industrial processes have reached their highest ever annual level of 36.3 Gt.[1] Recycle CO_2 by carbon capture and utilization (CCU) process is a sustainable route towards CO_2 emission control, since it can partially close the carbon cycle.[2] Hence, increasing attention is being paid to use CO_2 as a feedstock to produce carbon-containing products via homogeneous, bio-, photo-, electro- and thermal-catalytic pathways.[3] Among them, heterogeneous thermal catalysis is better adapted to the current industrial infrastructure, which is a key advantage to deploy CCU process at large scale.

The catalytic reduction of CO_2 by H_2 into hydrocarbon fuels and chemicals (i.e. hydrogenation) is considered as the most realistic and attractive solution for CO_2 recycling.[4] This is because the H_2 required for the reaction can be produced from water electrolysis using surplus wind and solar electric power, generated when the demands for energy are low. Therefore, the problems of CO_2 disposal and storage of intermittent renewable energy can be tackled together providing a net CO_2 removal from the atmosphere. Depending on the reaction conditions and the type of catalyst, CO_2 hydrogenation can produce a wide variety of target molecules, including carbon monoxide, hydrocarbons and alcohols. Methane production, via methanation, or elsewhere known as the Sabatier reaction, is widely explored as one of the potential Power-to-Gas (PtG) technologies to substitute natural gas (CH_4 is the majority component of natural gas) while promoting the interaction between gas and electric grids.[5] In addition, methane can be produced at relatively mild reaction conditions with high CO_2 conversion rates and almost 100% selectivity.[6]

As in many heterogeneous catalytic reactions, the typical CO_2 methanation catalyst configuration consists of an active metal dispersed over a high surface area oxide support. Group 8-10 transition metals are suitable catalyst for the reaction, with Ru and Ni being the most active and selective. [5–7] Ni possesses remarkable advantages relative to Ru for large scale industrial applications due to the comparable catalytic performance and much lower cost. A plethora of supporting materials has been studied for this reaction, extending from conventional zeolites to more elaborated configurations such as core/shell structures or metal–organic frameworks (MOFs).[5] Reducible oxides, such as TiO_2 and CeO_2 have been widely used as supports for CO_2 methanation and in almost all cases were found to enhance the catalytic performance as compared to more inert supports such as Al_2O_3 or SiO_2.[8,9] Among the many reducible supports, CeO_2 has attracted strong interest in the field of CO_2 valorisation because Ce^{4+} can be easily reduced to Ce^{3+} and create oxygen vacancy (O_V) sites.[10–12] The combination of the above

mentioned characteristics established CeO_2-supported Ni catalysts as one of the most studied and promising candidates for the CO_2 methanation reaction.[13,14]

Although the factors controlling the performance of Ni/CeO_2 methanation catalysts are far from being completely understood, there is consensus that the Ni particle size,[9,15–17] the interaction at the Ni-CeO_2 interphase[16,18,19] and the reducibility of ceria [20,21] are the most critical features of the catalyst. Despite the ongoing debate on the optimal Ni particle size,[8,9,15–17] there is general consensus that metallic Ni is essential for CO_2 methanation, while ionic Ni deteriorates the catalytic reaction.[22] In sharp contrast to this picture, in the present work, using well defined Ni-doped ceria nanoparticles as catalyst, we show that metallic nickel is not indispensable for the CO_2 methanation reaction. On the contrary, we found that ionic Ni species embedded into interstitial ceria lattice sites are not just active, but possess a record-high Ni mass-specific activity for CO_2 methanation reaction combined with very high CH_4 selectivity.

Results and Discussion

Catalytic tests

Figure1a shows the CO_2 conversion (X_{CO2}) and CH_4 product selectivity (S_{CH4}) of the $NiCeO_x$ catalyst measured in 2 independent experiments (exp. 1 and 2). Both parameters increase gradually with temperature and stabilize around 350 °C. For comparison, pure CeO_x shows negligible activity under identical conditions indicating that Ni-dopant is directly involved in the catalytic cycle. The maximum X_{CO2} (ca. 70%) is measured at 400 °C and is followed by S_{CH4} around 98%. The performance of Ni-doped ceria is comparable with that of supported Ni/CeO_2 catalysts containing 5 times higher Ni loading (around 10 % wt or even more).[23–25] Consequently the nickel mass-specific CO_2 conversion and CH_4 yield (right-axis in Figure 1a and 1b) are among the highest reported for Ni/CeO_2 catalysts (see Table S1). This is also confirmed by the comparison of the CO_2 conversion between doped and supported ceria catalysts containing the same Ni nominal loading, shown in Figure S3.

The activation energy of the CO_2 hydrogenation (E_a) was calculated from the Arrhenius plots, i.e., plots of the natural logarithm of the CO_2 consumption rate as a function of reciprocal temperature. As shown in Figure 1c the E_a is around 85 kJ/mol, which is among the lowest-reported for CO_2 methanation over Ni-based catalysts (typically around 120 kJ/mol)[26,27] suggesting facile activation of CO_2 over $NiCeO_x$, in line with the high mass-specific activity.

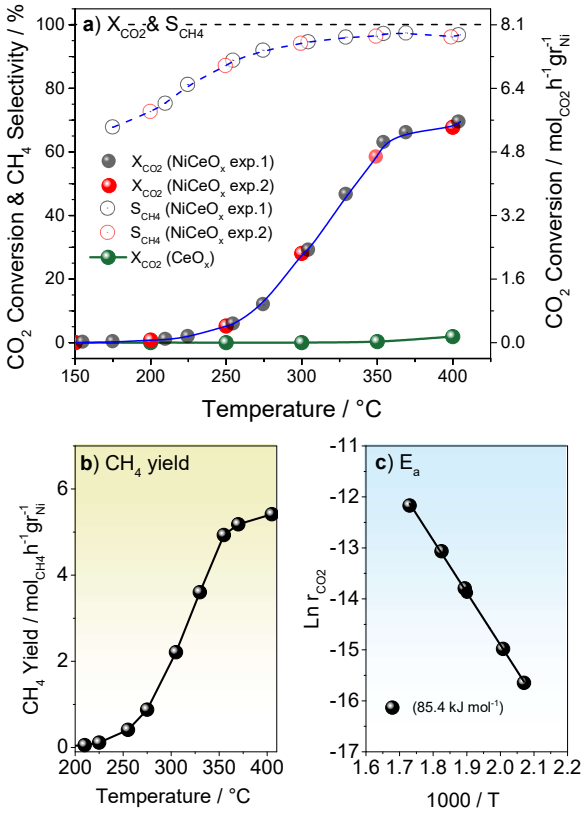

Figure 1. CO_2 methanation performance of $NiCeO_x$ and CeO_x catalysts as a function of temperature for two independent experiments (exp. 1 and 2) a) CO_2 conversion (X_{CO2}) and CH_4 selectivity (S_{SH4}). The X_{CO2} expressed as the overall CO_2 flow (%) (left y-axis) and normalized to the Ni loading (in $mol_{CO2}h^{-1}g_{Ni}^{-1}$) (right y-axis), b) the CH_4 yield expressed in $mol_{CH4}h^{-1}g_{Ni}^{-1}$ c) calculated CO_2 activation energy. Reaction conditions: CO_2:H_2 (1:4), GHSV=12000 h^{-1}, 1 bar.

Textural and physicochemical characterization of $NiCeO_x$

The BET specific surface area and the pore volume of calcined catalyst are 65 m^2 g^{-1} and 0.06 cm^3 g^{-1}, respectively (Table S2). The H_2-temperature-programmed reduction (H_2-TPR) profile of calcined $NiCeO_x$ is shown in Figure S4. On the grounds of previous reports[28–30] the TPR peak around 230 °C is ascribed to the reduction of adsorbed oxygen species while the peak at 275 °C contains the contribution of Ni-CeO_2 interface sites and highly dispersed NiO particles. Please note that NiO reduction peak shifts to higher temperature with the increase of particle size.[30]

The XRD profiles of calcined and H_2-activated (i.e. reduced) catalysts, shown in Figure S5, correspond to the ceria cubic fluorite phase (JCPDS 34e0394). Ni or NiO diffraction peaks are not detected suggesting high dispersion of Ni species, in accordance to previous results on Ni-doped ceria.[29,31] The crystallite size (d_{CeO2}), calculated by the Scherrer equation of the main (111) reflection peak (Table S2), for calcined catalyst was 6.1 nm and increases slightly after reduction to 7.5 nm. The ceria cubic fluorite lattice

parameter (α) of calcined catalyst is 5.414 Å which is somewhat higher than undoped ceria nanoparticles of similar sizes.[28,32] This indicates that Ni ions occupies interstitial positions in the ceria lattice (interstitial sites), since the substitution of Ce^{4+} lattice sites with the smaller Ni ions would have led to lattice contraction (i.e. decrease of α).[33] After reduction treatment the α parameter increases slightly to 5.418 Å which can be attributed to lattice expansion expected when Ce^{4+} cations are reduced to bigger ionic radius Ce^{3+}.

HR-TEM images of reduced $NiCeO_x$ catalyst show loosely packed crystalline ceria particles of rather small sizes (Figure 2a and Figure S6). Owing to the small contrast difference between Ni and CeO_2, STEM/EDX elemental mapping was used to distinguish the two phases. As shown in Figure 2b and 2d, Ni is homogenously distributed over ceria, while isolated Ni nanoparticles are also identified with mean particle sizes around 2 nm and quite narrow size distribution (Figure 2e). A significant concentration of atomically dispersed nickel can be distinguished in the higher magnification STEM/EDX image (Figure 2c) and confirmed by the EDX spectra (Figure 2f). These Ni clusters, which are too small to be considered in the Figure 2d histogram, constitute the majority of Ni sites and most likely correspond to Ni-dopant into ceria.

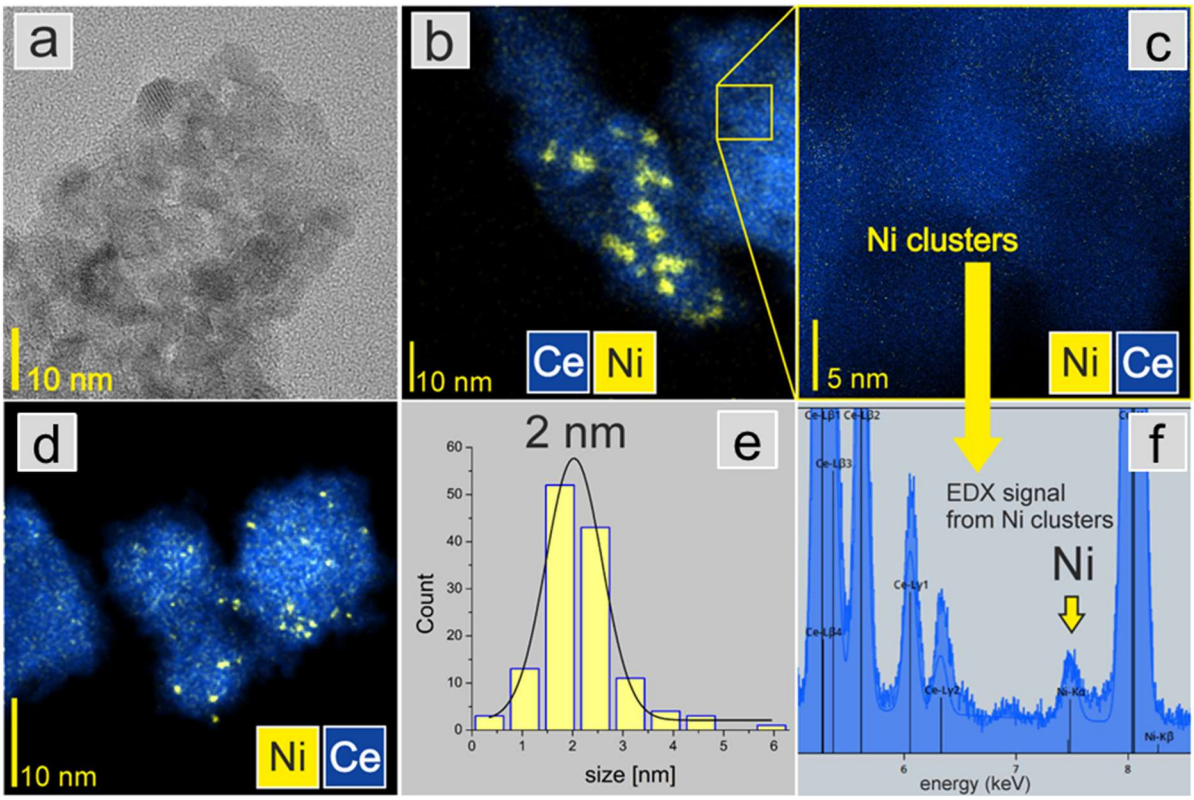

Figure 2. Microscopy images of reduced $NiCeO_x$ catalyst a) HR-TEM image, b), c) and d) STEM/EDX elemental mapping images with Ni and Ce signal overlay e) the corresponding particle-size distribution histogram (more than 100 particles analysed) and f) EDX spectrum from an area containing exclusively Ni clusters.

XANES and EXAFS measurements were used to obtain information on the local electronic structure and coordination environment of $NiCeO_x$ catalyst. The XANES spectra of oxidized and H_2-activated $NiCeO_x$, as well as those of Ni, NiO and Ni-Phthalocyanine (Ni-Ph, containing square planar Ni^{2+} species) reference samples, are shown in Figure 3a. The Ni K-edge of H_2-activated $NiCeO_x$ resembles that of NiO reference spectra implying that nickel remains largely oxidized after the H_2 treatment. Closer inspection of the Ni K-pre-edge (inset of Figure 3a) shows 3 characteristic structured features, indicated with the letters A, B and C in Figure 3a. The feature A, located at 8333 eV, is present in both octahedral and square planar coordinated Ni^{2+} ions and is associated to 1s→3d transition.[34,35] The features B and C at 8337.8 eV and 8340.6 eV respectively, are absent in NiO reference spectrum signifying that the structure of $NiCeO_x$ differs from the common octahedral NiO. According to literature the 1s→$4p_z$ pre-edge peak appears at 8338 eV for planar four-coordinated or pyramidal five-coordinated Ni^{2+} ion geometry (observable in Ni-Ph).[36] Accordingly, the component B could be attributed to Ni^{2+} 1s→$4p_z$ transition, while C might be related to Ni ions in oxidation state higher than 2.[37]

In case of H_2-activated $NiCeO_x$ is observed an increase in the global intensity of the rising-edge, followed by parallel drop of the white line peak, as compared to the oxidized sample. Comparison with the reference spectra suggests that these changes can be induced by superimposing spectral features related to metallic and/or square planar Ni^{2+} sites, both characterized by a broad-intense rising-edge and a flatter white line with respect to the octahedral NiO reference. Nevertheless, linear combination fit, using the reference spectra, could not satisfactorily reproduce the Ni K-edge of $NiCeO_x$ catalyst, possibly due to the nanostructured nature of $NiCeO_x$ phases.

Fourier transform (FT) EXAFS spectra offer parallel insights into the average coordination environment of Ni centres. The FT-EXAFS signal in the *R*-space 1-4 Å range (Figure 3b) contains the contribution of the first two coordination shells of Ni-O and Ni-Ni, respectively, originating either from NiO or from Ni coordinated with ceria lattice. The first coordination shell of oxidized $NiCeO_x$ is characterized by two components. The one at higher radial distance is found also in the NiO reference spectra, hence it can be related to Ni-O bonding of NiO particles ($Ni\text{-}O_{NiO}$).[38,39] The component at lower radial distance is absent in NiO reference, but clearly present also in the imaginary part of the FT-EXAFS (Figure S7). This component could be related to a Ni-O scattering paths from Ni species interacting with CeO_2 lattice sites ($Ni\text{-}O_{NiCe}$). A first-shell FT-EXAFS fit (Figure S9a-c) confirmed this qualitative assignment indicating the parallel presence of nanostructured NiO and interstitial Ni, the former with longer Ni-O bond than the latter (Table S4). In case of H_2-activated catalyst, the $Ni\text{-}O_{NiO}$ component is consumed while the $Ni\text{-}O_{NiCe}$ remains, suggesting higher stability of $Ni\text{-}O_{NiCe}$ species in reducing conditions.

The second-shell region of calcined $NiCeO_x$ presents a higher degree of complexity. Direct comparison with NiO reference compound allowed to identify the Ni-Ni_{NiO} scattering path. However, in case of $NiCeO_x$ this feature is shifted and presents a peculiar asymmetry at larger radial distances, suggesting the presence of 2 ionic Ni components. FT-EXAFS fitting up to 3.2 Å (Figure S9d-f) confirmed the presence of a Ni-Ce_{NiCe} scattering path at a significantly longer distance than the Ni-Ni_{NiO} one. Moreover, the FT-EXAFS fit allowed to quantify a 50:50 NiO:NiCe ratio. In parallel, the low coordination number (≈2) refined for the Ni-Ni_{NiO} scattering path indicated as NiO is present as small nanoparticles.

After H_2 treatment a component developed between first and second shell peaks, indicating the formation of metallic Ni-Ni, as also suggested from the XANES region. The complex nature and compositional characteristics of the system (high dilution of the Ni absorber in a heavily absorbing matrix, resulting in a limited resolution of the available EXAFS dataset), challenges quantitative EXAFS refinement. Yet, we attempted to fit the FT-EXAFS of reduced $NiCeO_x$ assuming full reduction of NiO nanoparticles to metallic Ni, even though part of NiO might be still present in the sample (Figure S9). The fit led to satisfactory results (Table S5), showing that a 50:50 Ni_{metal}:NiCe ratio is maintained, and suggesting indeed that most of NiO was reduced after reduction at 360 °C. Moreover, we identified a Ni-Ce_{NiCe} component at 3.10 Å, comparable with the results from calcined $NiCeO_x$ and in line with literature predictions of the Ni-Ce distance in the 2.8-3.2 Å range.[40] Nevertheless, it should be pointed out that FT-EXAFS fitting has a relatively high degree of uncertainty, due to high number of fitting parameters. Therefore dedicated studies are required in the future to fully unravel the local structure of Ni in NiCeO catalyst.

Overall, the analysis of XANES and EXAFS results yielded evidence for two types of Ni ions on $NiCeO_X$ with quite distinct reducibility under H_2. The first is easier to reduce and resembles to Ni^{2+} in NiO (hereafter abbreviated as NiO site), although its coordination environment is not alike to the standard octahedral bulk NiO. The second consists of Ni coordinated with oxygen atoms from ceria lattice (hereafter abbreviated as NiCe site). The NiCe is more difficult to reduce than NiO and according to XANES analysis is most likely in oxidation state higher than 2. On the basis of the STEM/EDX data of Figure 2 the NiO and NiCe sites are tentatively assigned to the 2 nm isolated Ni particles and the atomically dispersed Ni clusters on ceria, respectively.

The XANES Ce L_3-edge was used to examine the chemical state of ceria. As shown in Figure S11 the spectra of calcined and reduced $NiCeO_x$ are almost identical and very much similar to that of CeO_2 reference. This indicates that in the bulk the catalyst is not notably affected by the H_2 activation (i.e., reduction treatment) and remains stable as Ce^{4+}.

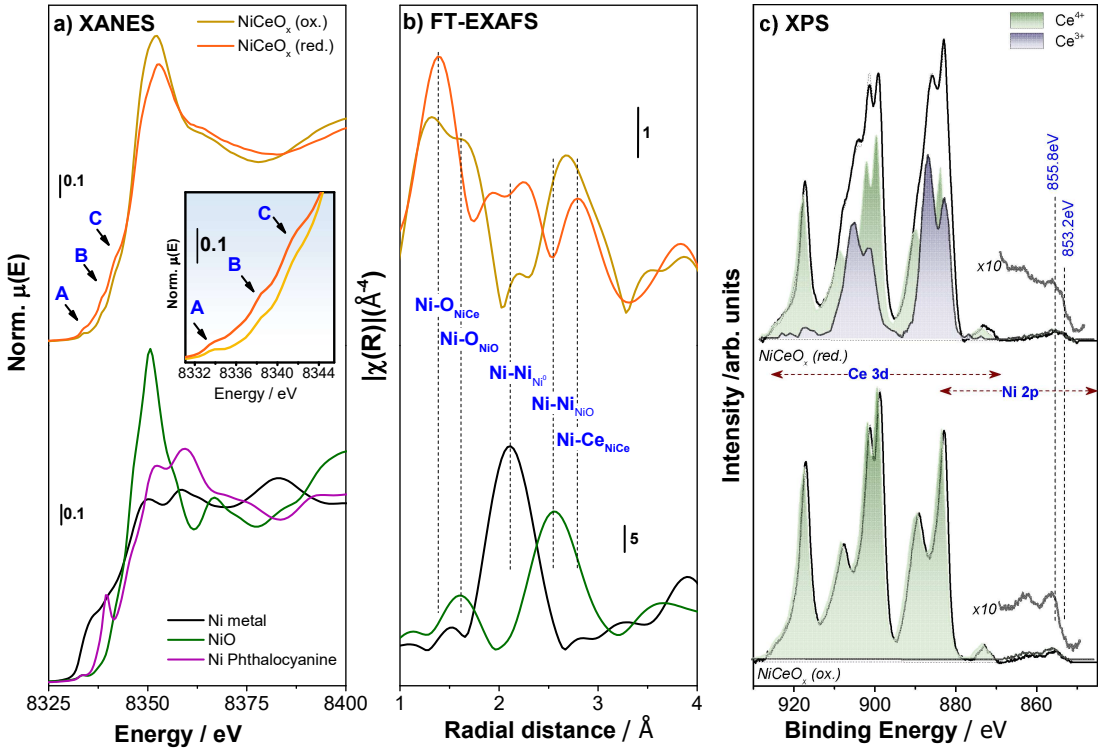

Figure 3 a) Ni K-edge XANES and b) k^3-FT-EXAFS spectra of oxidized/calcined ($NiCeO_x$ (ox.)) and H_2-activated ($NiCeO_x$ (red.)) $NiCeO_x$ catalysts *(top)* measured in fluoresce mode, as well as NiO, Ni metal and Ni-Phthalocyanine (square planar Ni^{2+} species) reference samples *(bottom)* measured in transmission mode c) Quasi in situ XPS Ce 3d and Ni 2p spectra (background subtracted) of oxidized and H_2-activated $NiCeO_x$, recorded in vacuum by using a monochromatic AlKα X-ray source. The Ce 3d peak is deconvoluted into Ce^{3+} and Ce^{4+} while the Ni $2p_{3/2}$ is magnified by 10 to better distinguish the spectral features.

The surface of calcined and H_2-activated $NiCeO_x$ was investigated in a laboratory XPS setup equipped with a reaction chamber (quasi in situ XPS). The Ce 3d and Ni $2p_{3/2}$ peaks of calcined catalyst (Figure 3c) correspond to the fully oxidized ceria and nickel states, respectively. After H_2 treatment the Ce 3d peak deconvolution suggests partial ceria reduction (Ce^{3+}:Ce^{4+} about 2:3), unlike to the XANES findings in Figure S11, where mainly Ce^{4+} was detected. This signifies that ceria reduction is limited at the surface, in accordance to the well-known surface reducibility of ceria by Ni dopants.[28,41]

The low Ni 2p signal does not allow reliable quantification of Ni oxidation state however, a component at 853.2 eV, characteristic to metallic nickel, appears after H_2-activation indicating partial Ni oxide reduction. The Ni atomic percentage, calculated from the Ni 2p/Ce 3d peak area ratio, is around 4% close to the nominal bulk composition (3.6 at.%) found by ICP-OES. The Ni 2p/Ce 3d ratio is practically unaffected after reduction, implying that the abundance of surface nickel sites is not drastically influenced. Accordingly, one can exclude extended migration of ceria species over Ni, previously reported for supported Ni/CeO_2 catalysts.[42]

Monitoring the $NiCeO_x$ surface evolution in CO_2 methanation reaction by operando sXAS

sXAS was employed to analyse the surface state of $NiCeO_x$ catalyst during CO_2 methanation at 1 bar gas pressure. It is important to underline that the surface sensitivity of sXAS is about 5 nm, thus comparable to XPS and much higher than XANES.[43] Figure 4a and 4b show characteristic Ni L_3 and Ce M_5-edge sXAS spectra respectively, recorded during H_2-activation and CO_2 methanation reaction. The complete set of Ni L_3 edges recorded during the light-off methanation tests as well as details on the fitting process can be found in section S9 of the Supporting Information. A clear modification of sXAS peaks in reaction mixture as compared to the prior state in H_2 is noticed, while the peak shape evolves as the temperature increases. The sXAS spectra are simulated by linear combination of reference peaks following the methodology developed in our recent work[28] (see also Figure S13). As shown in Figure 4a during H_2-activation nickel is partially reduced to Ni^0/NiCe (spectra at the light-blue background). Under reaction conditions and at low temperature nickel is oxidized to NiO/NiCe mixed state evidently due to the interaction with CO_2 in the gas phase.[44] As the temperature increases Ni^0 is formed in the expense of NiO. Notably, the sole nickel species constantly present throughout the reaction is NiCe.

The analysis of Ce M_5-edge (Figure 4b) reveals a redox evolution of ceria analogous to nickel. Specifically, the Ce^{3+} present in H_2, in the reaction mixture is oxidized initially to Ce^{4+}, before reducing back to Ce^{3+} at higher reaction temperature. Comparison between Figure 4a and 4b suggests a positive, almost linear, evolution of NiCe and Ce^{3+} components, implying that the two species are associated. As discussed before,[28] this behaviour can be explained by charge transfer from Ce^{4+} sites towards Ni^{2+} to form stable Ce^{3+}-$Ni^{\delta+}$ pairs ($2<\delta<3$).

On-line gas phase analysis of the sXAS cell via a micro gas chromatograph (GC) was used to connect the surface state with the catalytic performance. As shown in Figure 4c, X_{CO2} rises at around 230 °C and continuously increases up to 365 °C while S_{CH4} is initially very high (> 94%) but drops gradually above 310 °C. We should mention here that, despite its ability to operate in flow mode and at 1 bar gas pressure, the sXAS reactor has important differences from conventional fix-bed catalytic reactors since it is optimized for spectroscopy measurements (e.g. high reactor volume, reactants pass over and not through the catalyst, *etc.*). This justifies the much lower X_{CO2} as compared to the fixed-bed reactor experiments in Figure 1. Nevertheless, the evolution of X_{CO2} with temperature, as well as the high S_{CH4} are qualitatively similar in the two cases, which validates the correlation of catalytic and spectroscopic results.

The evolution of $\%Ce^{3+}$ and nickel species in the course of the reaction as obtained by sXAS spectra analysis is shown in Figure 4d. Ceria reduction starts at 280 °C and continues up to 365 °C. In case of

nickel, NiO dominates at low temperature, but above 270 °C it is gradually converted first to NiCe and then to a mixture of Ni^0 and NiCe. The formation of Ni^0 at 340 °C boosts the NiO transformation process. Comparison with the catalytic data in Figure 4c, indicates a positive correlation between $\%Ce^{3+}$ and X_{CO2} in the whole temperature range.

Despite the net increase of X_{CO2} in the 240-340°C region, the Ni L-edge analysis shows that nickel remains oxidized. Besides, formation of Ni^0 above 340 °C does not have a notable effect on X_{CO2} which continue to increase linearly with temperature. These findings seem to challenge the widely accepted conception that metallic nickel is indispensable for H_2 activation during methanation reaction. In order to examine if the reaction can take place at reduced ceria sites, we performed a reference sXAS methanation experiment on pure CeO_x nanoparticles. As shown in Figure S14, CeO_x is not active for CO_2 conversion, confirming the results of Figure 1. However, based on the operando Ce M_5 sXAS spectra, a significant population of Ce^{3+} species is present on the surface under these conditions (Figure S14). Therefore, the reactivity of Ce^{3+} species is negligible without the presence of Ni ions, suggesting that nickel, and particularly ionic nickel species, plays a key role in methanation reaction.

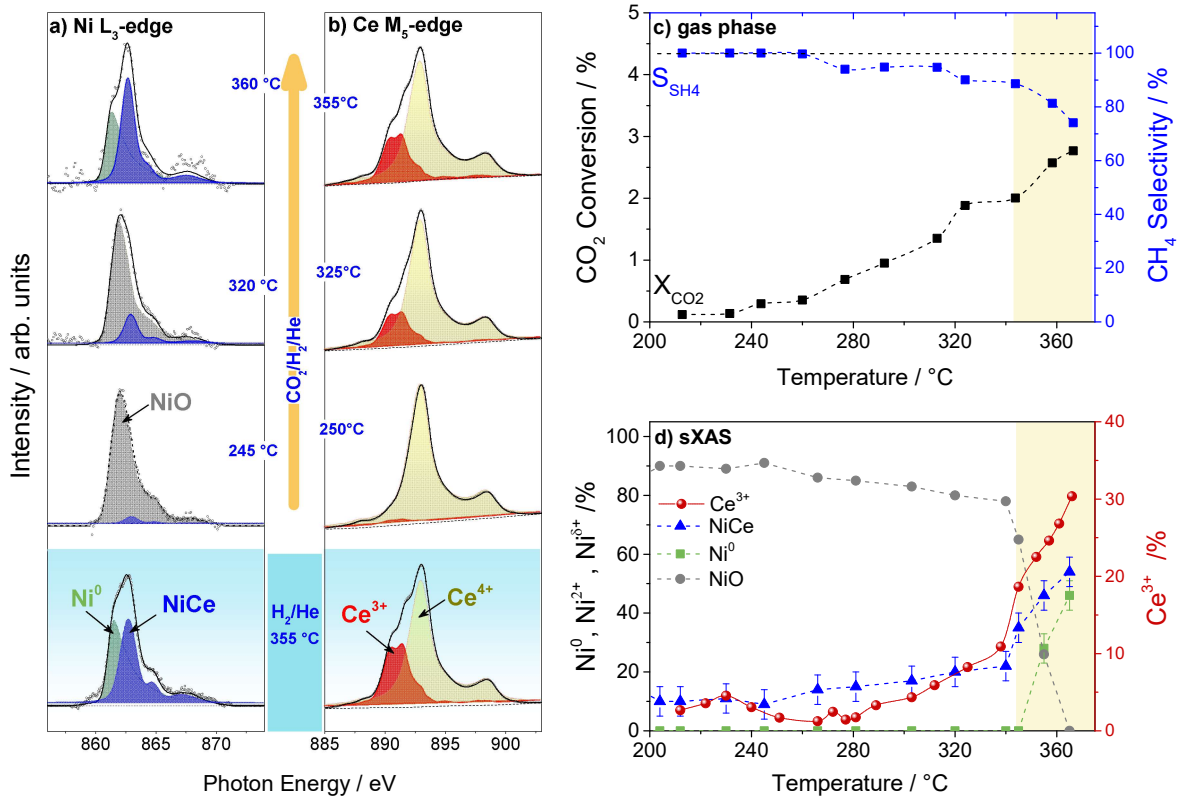

Figure 4. a) Ni L_3-edge and b) Ce M_5-edge sXAS spectra of $NiCeO_x$ catalyst under activation and light-off CO_2 methanation reaction, c) CO_2 conversion (X_{CO2}) and CH_4 selectivity (S_{SH4}) as a function of temperature measured in the sXAS cell by *on line* GC, d) the evolution of various nickel and ceria oxidation states in the course of CO_2 methanation reaction obtained by the analysis of Ni L_3 and Ce M_5-edges respectively. *Conditions*: activation in 1

bar 10% H_2/He at 355 °C, cooled down in H_2, introduction of CO_2:H_2:He (1:4:20) reaction mixture at 135 °C and temperature raise with a rate of 1.7 °C min^{-1}. Spectra coming from reference samples: metallic Ni^0 (green), NiO (gray), NiCe (blue), Ce^{4+} (dark yellow) and Ce^{3+} (red).

First principles calculations and APXPS experiments to rationalize the high activity of $NiCeO_x$ catalysts

The catalytic and spectroscopic results described above clearly show that surfaces containing ionic nickel species have considerable methanation activity per nickel mass, implying that metallic nickel is not indispensable, as it is usually anticipated for supported Ni/CeO_2 catalysts. In addition, partially reduced CeO_x is inactive towards CO_2 hydrogenation (Figure S14), indicating that Ce^{3+}-O_V pairs are not sufficient for methanation reaction. This observation put forward ionic Ni-Ce^{3+} pairs as efficient reaction sites, contrary to the commonly accepted notion that metallic Ni and Ce^{3+} are the active sites for CO_2 hydrogenation.[11,16,18,21–23,42,44] The rather unexpected reactivity scheme is interpreted on the grounds of first principles calculations combined with ambient pressure XPS experiments.

First, we address the stability of interstitial Ni sites over ceria. Based on previous HR-TEM results,[29] we have mainly considered for the calculations the CeO_2(111) and CeO_2(100) surfaces. An oxygen vacancy (O_v) was also introduced in these two models,[45] denoted as CeO_2(111)-O_v and CeO_2(100)-O_v, in Figure S15 and Figure 5a-b. This is required because the H_2 activation is likely to result in vacancies on ceria surface (O_vs), as suggested by the XPS and sXAS in Figure 3c and 4b, respectively. For CeO_2(100)-O_v, some Ce atoms are exposed, forming Ce-O frustrated Lewis pairs (FLP), displayed with an arrow in Figure 5a. There are 4 or 6 adsorption sites for generating interstitial Ni on CeO_2(111)-O_v (Figure S15a) or CeO_2(100)-O_v (Figure S15b), respectively. The calculated adsorption energy (Table S7) shows that the Ni atom is very stable when adsorbed on two adjacent oxygen atoms on CeO_2(100) surface, as its adsorption energy (-5.66 eV) is much larger than the cohesive energy of its bulk (-4.75 eV), which is consistent with that reported by Li et al.[46] The other adsorption configurations of the interstitial Ni on CeO_2(100), as well as on CeO_2(111), are much less stable and will not be considered thereafter in the calculations of H_2 and CO_2 interaction. For Ni-doped CeO_2(100)-O_v (Figure 5c, d), the combination of the exposed Ce with Ni generates a Ni-Ce pair with a distance of 3.18 Å and the Ni-O classical Lewis pair (CLP) has a distance of 1.77 Å, as shown by arrows in Figure 5c, both results are in line with FT-EXAFS fit results (Table S4). In addition, Bader charge analysis shows that Ni has a charge of +0.57 |e|, indicating its ionic nature. The above DFT results support the sXAS experiments (Figure 4a and 4d) which showed the formation of quite stable ionic nickel, in particular NiCe species, on $NiCeO_x$ catalyst.

We examine next the interaction of H_2 with CeO_2 and $NiCeO_2$, both containing O_v. Previous studies have demonstrated that H_2 dissociation at FLP sites often proceeds heterolytically to form both protonic and hydridic species.[41,47] On CeO_2(100)-O_v, H_2 is first physisorbed on the Ce-O FLP site and subsequently

dissociates heterolytically to produce Ce-H and O-H without an energy barrier (Figure 5e), suggesting that OH groups are readily formed on ceria upon H_2 exposure. This result is consistent with the calculated energy barrier (0.08 eV) of H_2 dissociation at the FLP site on CeO_2(100) reported in a previous work by Chang and co-workers.[47] Similar results can be found to occur on Ni-doped CeO_2(100)-O_v (Figure S16). On Ni-doped hydroxylated CeO_2(100), the Ni-Ce pair is unlikely to activate the H_2 molecule due to a large energy barrier of 1.80 eV (Figure S17). Instead, the Ni-O CLP can facilitate H_2 dissociation to generate Ni-H and O-H with a small energy barrier of 0.11 eV (Figure 5f), indicating that the interstitial Ni on CeO_2(100) can efficiently activate hydrogen. This finding is not only important to explain the reactivity of $NiCeO_x$ but can also rationalize our previous findings showing a net enhancement in the $NiCeO_X$ reducibility in H_2 as compared to CeO_x.[28]

For CO_2 activation, our DFT results show that CO_2 can be bound to surface OH groups on both hydroxylated-CeO_2(100) and Ni-doped hydroxylated-CeO_2(100) surfaces to form strongly adsorbed carbonate intermediates (E_{ads} is about -5 eV) (Figure 5g, h). According to the Sabatier principle, intermediates with either too strong or too weak adsorption are not favourable to catalytic reactions. Especially, strongly adsorbed carbonates are expected to block surface reaction sites, reducing the catalytic turnover. Interestingly, in contrast to hydroxylated-CeO_2(100), the Ni-doped hydroxylated-CeO_2(100) possesses an alternative Ni-Ce site for effective activation of CO_2, where the adsorbed CO_2 is bent by coordination of the C and O atoms to Ni and Ce, respectively (Figure 5i). In this case, CO_2 is found to have a moderate adsorption energy of -0.85 eV.

Furthermore, our calculations indicated that on the hydroxylated-CeO_2(100) surface Ni can be coordinated with four surface oxygen atoms (O_s) to form a square planar Ni (Figure S18a) with E_{ads} of -9.82 eV for the Ni atom, which is consistent with the experimental findings discussed above. However, the interstitial Ni in this structure allows only weak adsorption of CO_2 (E_{ads} = -0.30 eV) with a linear configuration (Figure S18b, c) and therefore cannot activate CO_2. This result is an evidence that the NiO species detected by sXAS and XANES (previously connected to square planar Ni^{2+} coordination sites[28]) do not affect the reactivity of $NiCeO_x$ and the reaction mainly takes place over NiCe and Ce^{3+} sites.

Bader charge analysis showed that the C atom in the adsorbed carbonate intermediate (Figure 5g-i) has a charge larger than +2 |e|. In contrast, the C atom of the adsorbed CO_2 on the Ni-Ce site has a less positive charge of +1.46 |e|, which is beneficial for promoting methanation by capturing H species, leading to methanation. To sum up, the DFT calculations confirm that the experimentally observed ionic state of Ni is essential in H_2 dissociation and CO_2 activation.

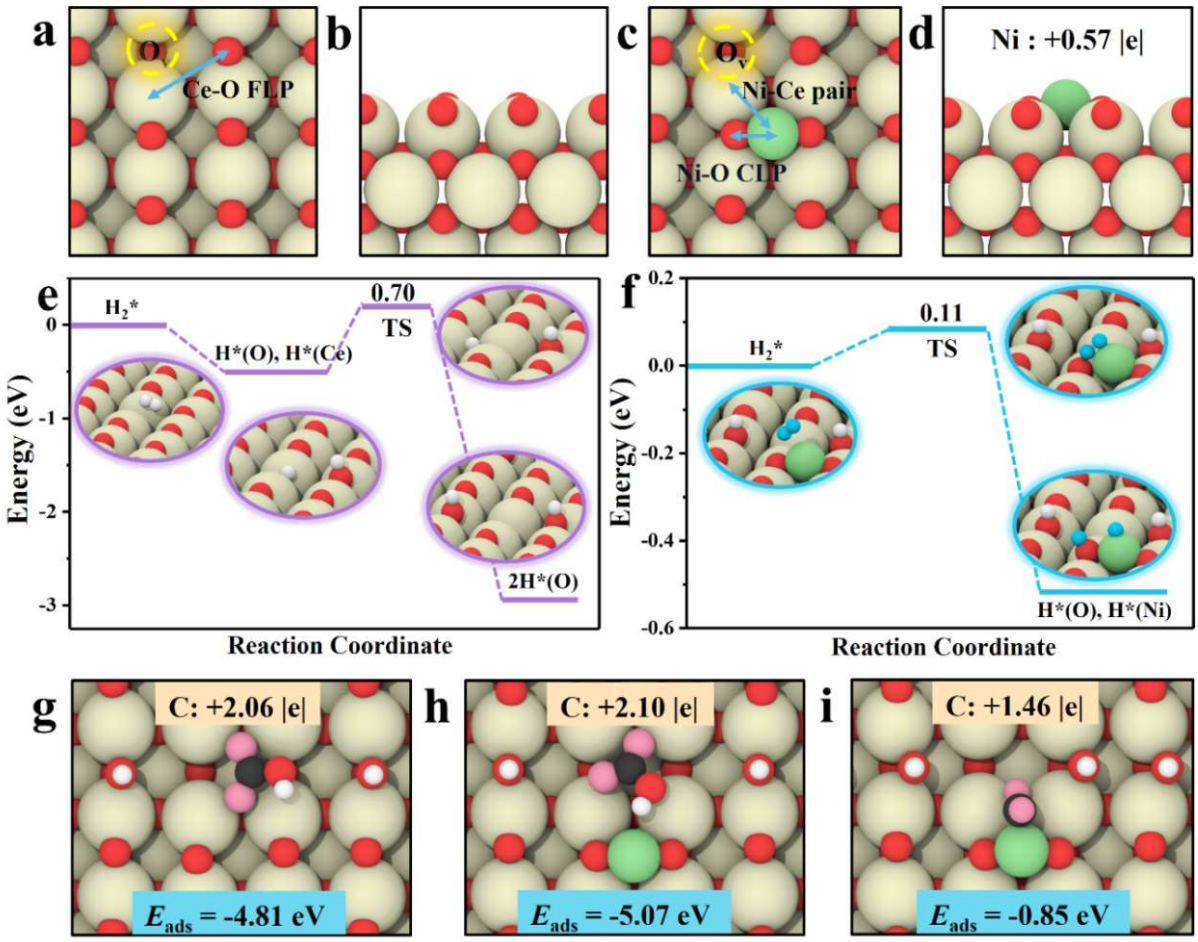

Figure 5. Top (a) and side (b) views of the CeO_2(100) surface with an O_v site (yellow circle). Top (c) and side (d) views of the Ni-doped CeO_2(100) surface with an O_v site (yellow circle). The Ce-O frustrated Lewis pair (FLP), Ni-O classical Lewis pair (CLP), and the Ni-Ce pair sites are marked with arrows. The Bader charge of Ni is also labeled. e) Reaction pathway for dissociation of H_2 at the Ce-O FLP and migration of H from Ce to nearby surface O on hydroxylated CeO_2(100). f) Reaction pathway for dissociation of H_2 at the Ni-O CLP site on Ni-doped hydroxylated CeO_2(100). Adsorption of CO_2 to form carbonate intermediate on (g) hydroxylated CeO_2(100), (h) Ni-doped hydroxylated CeO_2(100), and adsorption of CO_2 (i) at the Ni-Ce pair site of Ni-doped hydroxylated CeO_2(100). The Bader charge of C and adsorption energy (E_{ads}) is also labeled. *Color scheme*: Ni, green; Ce, yellow; surface O, red; O in CO_2, pink; H, white or blue; C, black. The adsorbed species are denoted with asterisks (*).

In situ ambient pressure XPS (APXPS) experiments were performed to verify the key findings of DFT calculations. To this scope, the CeO_x and $NiCeO_x$ catalysts were examined in 2 mbar O_2, H_2 and mixed CO_2:H_2 (1:4) ambient under isobaric conditions, focusing on the type and the amount of surface adsorbates. The O 1s spectra of the two catalysts (Figure 6a) show a quite complex line shape. The intense peak around 530 eV is characteristic of bulk-like ceria lattice oxygen (O_{lat}),[48–50] while the shoulder on the high BE side is assigned to oxygenated adsorbates (O_{ads}).[48,50–53] Depth-dependent photoemission measurements (Figure S19) show a clear enhancement of O_{lat} signal with the analysis depth, confirming the assignment above. In O_2 atmosphere O_{lat} dominates the O 1s spectra, while in H_2 and CO_2:H_2 there is clear development of the O_{ads} spectral features. The best fitting of the O 1s spectrum

is obtained using 4 individual peaks centered (±0.2 eV) at 530.1, 531.2, 532.3 and 533.9 eV. Based on earlier photoemission and computational studies we can safely assign the peak at 530.1 eV to O_{lat} and those at 532.3 and 533.9 eV to OH^- groups and adsorbed H_2O species, respectively.[48–50] The peak at 531.2 eV may originate from several species, such as OH-H_2O pairs,[53] carbonates[53] or O-bonded to silicon impurities[54] (Figure S20). From the above presented analysis it is clear that both surfaces can effectively accommodate OH^- species in H_2 atmosphere, in agreement with the DFT prediction that H_2 readily dissociates over Ce-O FLP and Ni-O CLP surface sites (Figures 5e and S16).

The amount of Ce^{3+} species, as this is calculated by the deconvoluted Ce 3d spectra (examples of Ce 3d spectra deconvolution are given in Figure S21), is direct measure of the surface oxygen vacancies (O_V) and thus proportional to the Ce-O FLP sites. According to the DFT results, on pure ceria OH^- groups are formed on Ce-O FLP, while in case of $NiCeO_x$ the Ni-O CLP offer additional dissociation sites (Figure 5f). The OH^- to Ce^{3+} peak area ratio (OH^-/Ce^{3+}) obtained from the O 1s and Ce 3d peak analysis, can help to verify this point. In particular, if hydroxyls are exclusively formed on O_V sites, then OH^-/Ce^{3+} should be the same for both samples. Apparently, this is not the case, since the OH^-/Ce^{3+} is systematically higher for $NiCeO_X$ (Figure S22a), suggesting that this sample contains additional locations that can accommodate OH^- groups. In other worlds, OH^- can be formed on sites other than O_V. These "additional" sites correspond well to the Ni-O CLP proposed by the DFT calculations, making $NiCeO_x$ catalyst very efficient to H_2 activation.

We turn now our attention to the interaction of CO_2 with the two samples. DFT calculations anticipate the formation of strongly adsorbed carbonate species (CO_3^{2-}) when hydroxylated CeO_x and $NiCeO_X$ surfaces are exposed to CO_2. In order to test this finding, we present in Figure 6b the C 1s spectra of the two samples recorded in O_2, H_2 and CO_2:H_2 atmospheres. The absence of C 1s peak in O_2 (spectra at the bottom of Figure 6b) suggests that both catalysts were initially clean from carbon impurities. Therefore, the C 1s peak appeared in H_2 and CO_2:H_2 originates from the interaction with the gas phase. Please note that the C 1s signal detected in H_2 gas is due to preceding CO_2 exposure tests (included in Table S8). The most intense C 1s peak around 290.5 eV is characteristic of carbonates,[55,56] in full agreement with the predictions of DFT calculations. The C 1s peaks at 286.6 (CeO_x) and 285.5 eV ($NiCeO_X$) it could be attributed to methoxy (CH_3O-) or carboxylate (-CO_2-) species.[56] These species contribute to about 20% of the overall adsorbed carbon and might be either the product of carbonates decomposition or actively participate to the reaction.

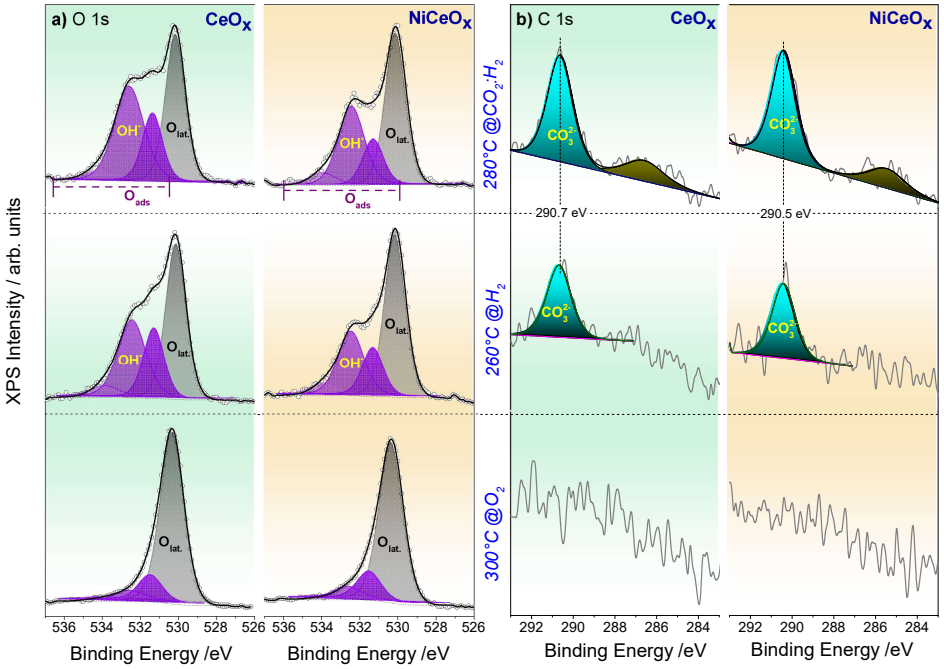

Figure 6. a) APXPS O 1s spectra of CeO_x (left) and $NiCeO_x$ (right) catalysts measured with 710 eV photon energy (estimated probing depth ca. 2.5 nm) at the indicated conditions. The O 1s spectra are fitted with 4 components by applying appropriate constrains described in the text. For easier comparison of the peak shapes the intensity is normalized to the same height. b) C 1s spectra of CeO_x (left) and $NiCeO_x$ (right) catalysts measured with 465 eV photon energy at the indicated conditions. The C 1s spectra are fitted with 2 components. In all cases the binding energy scale is calibrated to the Ce 4f peak of reduced ceria (at 2.0 eV) or O 2p peak of oxidized ceria (at 4.5 eV) recorded with the same photon energy.

Quantitative analysis did not show clear differences in the surface concentration of carbonates species between the two catalysts (Figure S22b). However, systematic C 1s measurements (see S23 and Table S8 for details) revealed a small (0.2 eV), but reproducible BE shift of the CO_3^{2-} peak between the two catalysts. In particular, the mean BE was 290.69 (0.08) eV and 290.48 (0.10) eV (in parentheses are the standard deviation relative to the mean value) for CeO_x and $NiCeO_x$ catalysts, respectively. Previous computational studies of carbonates have shown that the BE of the C 1s shifts to higher values as the charge of the C atom is more positive.[57] Consequently, the lower BE of carbonates over $NiCeO_x$ as compared to CeO_x supports the Bader charge analysis results (Figure 5g-i) which showed that adsorbed CO_2 on the Ni-Ce sites has less positive charge, which in turn is beneficial for methanation reaction.

Gas phase analysis in the APXPS chamber using *on line* mass spectrometer did not show detectable activity, which not surprising considering the relatively low pressure (2 mbar) of the catalytic reaction. Therefore, despite the fact the samples were measured in CO_2:H_2 reaction mixtures, the catalytic turnover at the surface sites is very low, if any, which prevents any conclusion about the influence of carbonate species in the reaction. Nevertheless, APXPS proves itself as a fine analysis technique able to

compare the surface species formed in the two cases and provides solid experimental evidence to support the DFT predictions.

Conclusion

In this work, Ni-doped ceria nanoparticles prepared by the soft templating method were investigated as CO_2 hydrogenation catalysts, displaying one of the highest ever reported Ni mass-specific activities and almost 100% methane selectivity. Stable ionic Ni species, associated with interstitial Ni atoms in contact with Ce^{3+} lattice are identified as very active sites for CO_2 conversion, indicating that metallic nickel is not indispensable for CO_2 hydrogenation. First principles calculations confirm the stability of interstitial ionic Ni on ceria surfaces and explain how they promote H_2 dissociation and CO_2 activation. The theoretical results were validated by in situ APXPS analysis of Ni-doped and pure ceria catalysts under H_2-activation and CO_2 hydrogenation reaction conditions. We believe that this new paradigm of Ni-Ce pair active sites might also applied to other type of ceria-based catalysts and possibly diverse oxide-catalyzed hydrogenation reactions, providing the design principles that could lead to more effective catalysts in the future.

Acknowledgments

M.B and S.Z acknowledge the support of the French Agence Nationale de la Recherche (ANR), under the projects DuCaCO2 (No236294) and CELCER-EHT. J.Z. would like to thank the China Scholarship Council (CSC) for supporting his stay at ICPEES. This work received financial support from CALIPSOplus project under the proposal number 20200271 from the EU Framework Program HORIZON 2020. We acknowledge Elettra for the allocation of synchrotron radiation beamtime and the APE-HE beamline staff for the collaboration during the experiments. The authors are grateful to D. Bernasconi for the support and Dr. O. Mathon for the precious collaboration during the XAS experiments. We acknowledge SOLEIL for provision of synchrotron radiation facilities and SOLEIL staff for the assistance in using TEMPO beamline. We thank Prof. C. Petit for the useful and constructive discussions and Dr S. Labidi for the support with the catalytic measurements. J.L. and S.L. acknowledge support from National Natural Science Foundation of China (21973013 to S.L.) and National Natural Science Foundation of Fujian Province, China (2020J02025 to S.L.). Finally, H.G. thanks the Air Force Office of Scientific Research for support under grant No. FA9550-22-1-0350 (H.G.).

References

[1] *IEA (2022), Global Energy Review: CO2 Emissions in 2021*, Paris, **2022**.

[2] S. M. Jarvis, S. Samsatli, *Renewable and Sustainable Energy Rev.* **2018**, *85*, 46–68.

[3] E. Cheol Ra, K. Young Kim, E. Hyup Kim, H. Lee, K. An, J. Sung Lee, *ACS Catal.* **2020**, *10*, 11318–11345.

[4] S. De, A. Dokania, A. Ramirez, J. Gascon, *ACS Catal.* **2020**, *10*, 14147–14185.

[5] I. Hussain, A. A. Jalil, N. S. Hassan, M. Y. S. Hamid, *J. Energy Chem.* **2021**, *62*, 377–407.

[6] J. Ashok, S. Pati, P. Hongmanorom, Z. Tianxi, C. Junmei, S. Kawi, *Catal. Today* **2020**, *356*, 471–489.

[7] Z. Zhang, C. Shen, K. Sun, X. Jia, J. Ye, C. J. Liu, *J. Mater. Chem. A* **2022**, *10*, 5792–5812.

[8] J. Liu, X. Wu, Y. Chen, Y. Zhang, T. Zhang, H. Ai, Q. Liu, *Int. J. Hydrogen Energy* **2022**, *47*, 6089–6096.

[9] Z. Hao, J. Shen, S. Lin, X. Han, X. Chang, J. Liu, M. Li, X. Ma, *Appl. Catal. B* **2021**, *286*, 119922.

[10] K. Chang, H. Zhang, M. J. Cheng, Q. Lu, *ACS Catal.* **2020**, *10*, 613–631.

[11] Y. Xie, J. Wen, Z. Li, J. Chen, Q. Zhang, P. Ning, Y. Chen, J. Hao, *Green Chem.* **2023**, *25*, 130–152.

[12] D. R. Mullins, *Surf. Sci. Rep.* **2015**, *70*, 42–85.

[13] Y. Dai, M. Xu, Q. Wang, R. Huang, Y. Jin, B. Bian, C. Tumurbaatar, B. Ishtsog, T. Bold, Y. Yang, *Appl. Catal. B* **2020**, *277*, 119271.

[14] G. Zhou, H. Liu, K. Cui, A. Jia, G. Hu, Z. Jiao, Y. Liu, X. Zhang, *Appl. Surf. Sci.* **2016**, *383*, 248–252.

[15] L. Lin, C. A. Gerlak, C. Liu, J. Llorca, S. Yao, N. Rui, F. Zhang, Z. Liu, S. Zhang, K. Deng, C. B. Murray, J. A. Rodriguez, S. D. Senanayake, *J. Energy Chem.* **2021**, *61*, 602–611.

[16] G. Varvoutis, M. Lykaki, S. Stefa, V. Binas, G. E. Marnellos, M. Konsolakis, *Appl. Catal. B* **2021**, *297*, 120401.

[17] C. Vogt, E. Groeneveld, G. Kamsma, M. Nachtegaal, L. Lu, C. J. Kiely, P. H. Berben, F. Meirer, B. M. Weckhuysen, *Nat. Catal.* **2018**, *1*, 127–134.

[18] S. Lin, Z. Li, M. Li, *Fuel* **2023**, *333*, 126369.

[19] C. Alvarez-Galvan, P. G. Lustemberg, F. E. Oropeza, B. Bachiller-Baeza, M. Dapena Ospina, M. Herranz, J. Cebollada, L. Collado, J. M. Campos-Martin, V. A. De La Peña-O'shea, J. A. Alonso, M. V. Ganduglia-Pirovano, *ACS Appl. Mater. Interfaces* **2022**, *14*, 50739–50750.

[20] S. Hu, L. Zhang, Z. Cao, W. Yu, P. Zhang, X. Zhu, W. Yang, *J. Power Sources* **2021**, *485*, 229343.

[21] S. Tada, H. Nagase, N. Fujiwara, R. Kikuchi, *Energy Fuels* **2021**, *35*, 5241–5251.

[22] T. S. Galhardo, A. H. Braga, B. H. Arpini, J. Szanyi, R. V. Gonçalves, B. F. Zornio, C. R. Miranda, L. M. Rossi, *J. Am. Chem. Soc.* **2021**, *143*, 4268–4280.

[23] A. Cárdenas-Arenas, A. Quindimil, A. Davó-Quiñonero, E. Bailón-García, D. Lozano-Castelló, U. De-La-Torre, B. Pereda-Ayo, J. A. González-Marcos, J. R. González-Velasco, A. Bueno-López, *Appl. Mater. Today* **2020**, *19*, 100591.

[24] Y. Du, C. Qin, Y. Xu, D. Xu, J. Bai, G. Ma, M. Ding, *Chem.Eng. J.* **2021**, *418*, 129402.

[25] R.-P. Ye, Q. Li, W. Gong, T. Wang, J. J. Razink, L. Lin, Y.-Y. Qin, Z. Zhou, H. Adidharma, J. Tang, A. G. Russell, M. Fan, Y.-G. Yao, *Appl. Catal. B* **2020**, *268*, 118474.

[26] A. I. Tsiotsias, N. D. Charisiou, A. AlKhoori, S. Gaber, V. Stolojan, V. Sebastian, B. van der Linden, A. Bansode, S. J. Hinder, M. A. Baker, K. Polychronopoulou, M. A. Goula, *J. Energy Chem.* **2022**, *71*, 547–561.

[27] K. Jalama, *Catal. Rev.* **2017**, *59*, 95–164.

[28] M. Barreau, D. Chen, J. Zhang, V. Papaefthimiou, C. Petit, D. Salusso, E. Borfecchia, S. Turczyniak-Surdacka, K. Sobczak, S. Mauri, L. Braglia, P. Torelli, S. Zafeiratos, *Mater. Today Chem.* **2022**, *26*, 101011.

[29] W. Derafa, F. Paloukis, B. Mewafy, W. Baaziz, O. Ersen, C. Petit, G. Corbel, S. Zafeiratos, *RSC Adv.* **2018**, *8*, 40712–40719.

[30] Y. Xie, J. Chen, X. Wu, J. Wen, R. Zhao, Z. Li, G. Tian, Q. Zhang, P. Ning, J. Hao, *ACS Catal.* **2022**, *12*, 10587–10602.

[31] H. Shen, Y. Dong, S. Yang, Y. He, Q. Wang, Y. Cao, W. Wang, T. Wang, Q. Zhang, H. Zhang, *Nano Res.* **2022**, *15*, 5831–5841.

[32] D. Prieur, W. Bonani, K. Popa, O. Walter, K. W. Kriegsman, M. H. Engelhard, X. Guo, R. Eloirdi, T. Gouder, A. Beck, T. Vitova, A. C. Scheinost, K. Kvashnina, P. Martin, *Inorg. Chem.* **2020**, *59*, 5760–5767.

[33] D.-K. Lim, N. W. Kwak, J.-S. Kim, H. Kim, B.-K. Kim, Y.-C. Kim, W. Jung, *Acta Mater.* **2021**, *219*, 117252.

[34] A. Anspoks, A. Kuzmin, in *J. Non Cryst. Solids*, North-Holland, **2011**, pp. 2604–2610.

[35] W. Gu, S. Gencic, S. P. Cramer, D. A. Grahame, *J. Am. Chem. Soc.* **2003**, *125*, 15343–15351.

[36] G. J. Colpas, M. J. Maroney, C. Bagyinka, M. Kumar, W. S. Willis, S. L. Suib, N. Baidya, P. K. Mascharak, *Inorg. Chem.* **1991**, *30*, 920–928.

[37] W. Gu, H. Wang, K. Wang, *Dalton Trans.* **2014**, *43*, 6406–6413.

[38] N. Rui, X. Zhang, F. Zhang, Z. Liu, X. Cao, Z. Xie, R. Zou, S. D. Senanayake, Y. Yang, J. A. Rodriguez, C. J. Liu, *Appl. Catal. B* **2021**, *282*, 119581.

[39] Z. Zhang, K. Feng, B. Yan, *Catal. Sci. Technol.* **2022**, *12*, 4698–4708.

[40] Z. Chafi, N. Keghouche, C. Minot, *Surf. Sc.i* **2007**, *601*, 2323–2329.

[41] C. Riley, S. Zhou, D. Kunwar, A. De La Riva, E. Peterson, R. Payne, L. Gao, S. Lin, H. Guo, A. Datye, *J. Am. Chem. Soc.* **2018**, *140*, 12964–12973.

[42] T. Pu, J. Chen, W. Tu, J. Xu, Y.-F. F. Han, I. E. Wachs, M. Zhu, *J. Catal.* **2022**, *413*, 821–828.

[43] C. Castán-Guerrero, D. Krizmancic, V. Bonanni, R. Edla, A. Deluisa, F. Salvador, G. Rossi, G. Panaccione, P. Torelli, *Rev. Sci. Instrum.* **2018**, *89*, 054101.

[44] C. Heine, B. A. J. Lechner, H. Bluhm, M. Salmeron, *J. Am. Chem. Soc.* **2016**, *138*, 13246–13252.

[45] X. Lu, W. Wang, S. Wei, C. Guo, Y. Shao, M. Zhang, Z. Deng, H. Zhu, W. Guo, *RSC Adv.* **2015**, *5*, 97528–97535.

[46] W. Q. Li, S. Goverapet Srinivasan, D. R. Salahub, T. Heine, *Phys. Chem. Chem. Phys.* **2016**, *18*, 11139–11149.

[47] Z. Q. Huang, L. P. Liu, S. Qi, S. Zhang, Y. Qu, C. R. Chang, *ACS Catal.* **2018**, *8*, 546–554.

[48] Z. Liu, T. Duchoň, H. Wang, D. C. Grinter, I. Waluyo, J. Zhou, Q. Liu, B. Jeong, E. J. Crumlin, V. Matolín, D. J. Stacchiola, J. A. Rodriguez, S. D. Senanayake, *Phys. Chem. Chem. Phys.* **2016**, *18*, 16621–16628.

[49] D. R. Mullins, S. H. Overbury, D. R. Huntley, *Surf. Sci.* **1998**, *409*, 307–319.

[50] Z. Li, K. Werner, K. Qian, R. You, A. Płucienik, A. Jia, L. Wu, L. Zhang, H. Pan, H. Kuhlenbeck, S. Shaikhutdinov, W. Huang, H. J. Freund, *Angew. Chem. Int. Ed.* **2019**, *58*, 14686–14693.

[51] H. S. Casalongue, S. Kaya, V. Viswanathan, D. J. Miller, D. Friebel, H. A. Hansen, J. K. Nørskov, A. Nilsson, H. Ogasawara, *Nat. Commun.* **2013**, *4*, 2817.

[52] Z. Zeng, J. Greeley, *Nano Energy* **2016**, *29*, 369–377.

[53] N. Bosio, A. Schaefer, H. Grönbeck, *J. Phys.: Condens. Matter.* **2022**, *34*, 174004.

[54] Z. A. Feng, F. El Gabaly, X. Ye, Z. X. Shen, W. C. Chueh, *Nat. Commun.* **2014**, *5*, 4374.

[55] L. Zhong, M. Barreau, V. Caps, V. Papaefthimiou, M. Haevecker, D. Teschner, W. Baaziz, E. Borfecchia, L. Braglia, S. Zafeiratos, *ACS Catal.* **2021**, *11*, 5369–5385.

[56] Z. Liu, D. C. Grinter, P. G. Lustemberg, T. D. Nguyen-Phan, Y. Zhou, S. Luo, I. Waluyo, E. J. Crumlin, D. J. Stacchiola, J. Zhou, J. Carrasco, H. F. Busnengo, M. V. Ganduglia-Pirovano, S. D. Senanayake, J. A. Rodriguez, *Angew. Chem. Int. Ed.* **2016**, *55*, 7455–7459.

[57] M. Ebadi, A. Nasser, M. Carboni, R. Younesi, C. F. N. Marchiori, D. Brandell, C. M. Araujo, *J. Phys. Chem. C* **2019**, *123*, 347–355.

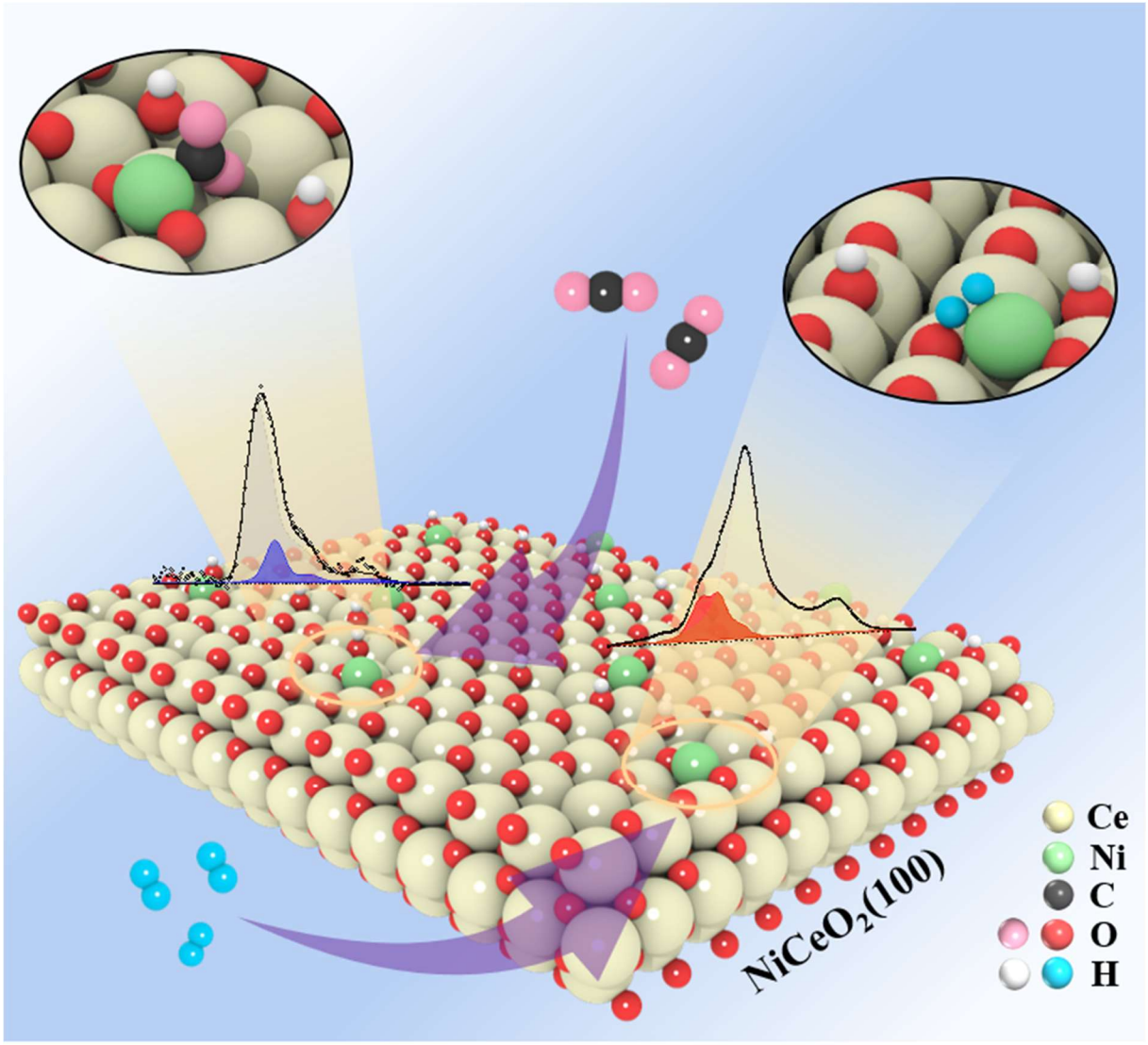

Ni-doped CeO_2 nanoparticles were synthesized and tested for CO_2 hydrogenation to CH_4 showing high Ni mass-specific activity and CH_4 selectivity. Operando spectroscopy combined with theoretical calculations identified ionic Ni species embedded in ceria as the catalytically active centers. Installation of highly dispersed ionic Ni species in the oxide matrix achieved a heterogeneous catalyst with high performance.